X-ray scattering in full-field digital mammography

Kirsi Nykänen[a] and Samuli Siltanen
Instrumentarium Corp., Imaging Div., P.O. Box 20, Tuusula, 04301, Finland

(Received 2 December 2002; accepted for publication 29 April 2003; published 25 June 2003)

Effects of x-ray scattering on full-field digital mammography are analyzed with the scattering model of Seibert and Boone [Med. Phys. **15**, 567–575 (1988)]. A new method is introduced for the estimation of model parameters from measurements. It is shown that with breasts thinner than a certain threshold, removing the anti-scatter grid leads to an improved contrast-to-noise ratio with a smaller patient dose. A fast approximate algorithm is presented for determining the scattered field in a gridless digital mammogram. © *2003 American Association of Physicists in Medicine.*
[DOI: 10.1118/1.1584160]

I. INTRODUCTION

Breast cancer is the most common cancer among women in Western countries.[1,2] X-ray mammography is the most frequently used diagnostic tool for the early detection of breast cancer. Signs of cancer in mammograms can be very subtle, and the image quality must be as good as possible. One of the major factors that lower the contrast resolution of mammographic images is x-ray scattering from breast tissue.

Anti-scatter grids are regularly used to absorb scattered x-rays in mammography. Problems with such a grid include the partial absorption of primary radiation, partial transparency to scattered x-rays, grid line artifacts, poor efficiency with increased patient dose, the need for designing mechanical movements and toxic material. Moreover, grids require an almost fixed direction of radiation and thus prevent three-dimensional (3-D) or stereo mammographic imaging.

Currently, digital mammography is becoming a viable alternative to conventional screen-film mammography, allowing the efficient use of digital image processing tools. Our purpose in this paper is to answer the following questions:

(1) Can one take a digital mammogram without a grid and remove the effect of scattered radiation from the image by postprocessing? Can patient dose be lowered this way without compromising image quality?
(2) Given a gridless digital mammogram and imaging parameters, how does one determine the scattered field?

Our answers to these questions are based on the convolution-based scattering model introduced by Seibert and Boone[4] and refined by Cooper, Boone, Seibert and Pellot-Bakarat.[5] We make a new contribution to this model by improving the determination of model parameters from measurements.

The answer to question (1) is partly affirmative. The scattered field is a low-frequency signal, so it does not introduce sharp artifacts.[5] Any trend removal algorithm or other gray-scale optimization removes the scattered field from the image. However, scattering reduces the contrast-to-noise ratio (CNR) since it narrows the dynamic range available for the diagnostically relevant primary signal. We show that for breasts thinner than a certain threshold, dose reduction is possible while maintaining the CNR.

To answer question (2), we present a fast approximate method for calculating the scattered field in a digital mammogram. The method is noniterative, robust against noise and works for any scatter-to-primary ratio. Furthermore, it is computationally effective since it is based on fast Fourier transform (FFT). We demonstrate the method with a simulated mammogram and apply it to a clinical full-field digital mammogram acquired with a new digital flat panel detector based on amorphous selenium.[6] Applications of the method include 3-D mammography and dual-energy breast imaging.

II. MATERIALS AND METHODS

A. Scattering models

Consider an (unrealistic) x-ray image of breast tissue with constant thickness taken without a scatter-prevention grid. Assume that all detected radiation passed through breast tissue, i.e., there was no open field. We call such images *ideal mammograms*.

Let us recall the scattering model of Boone and Seibert[4] applicable for ideal mammograms. Denote the mammogram by m and its pixel values by $m[i,j]$ for $i=1,\ldots,I$ and $j=1,\ldots,J$. Each pixel value is directly proportional to the number of x-ray quanta, both primary and scattered, detected by the pixel. According to Boone and Seibert, m is of the form

$$m = cx + p*x + \varepsilon, \tag{1}$$

where x is the scatter-free image, cx is the primary field, $p*x$ is the scattered field and ε is measurement noise. The number c satisfies $0<c<1$ and represents the fraction of primary radiation in m.

The function p is the 2-D scatter point spread function (scatter PSF) depending on the following parameters:[3]

- energy spectrum of the X-radiation,
- thickness of the breast tissue,
- x-ray beam field size

and

- the density of the breast tissue.

We denote by $*$ the usual two-dimensional convolution,

 0094-2405/2003/30(7)/1864/10/$20.00 © 2003 Am. Assoc. Phys. Med.

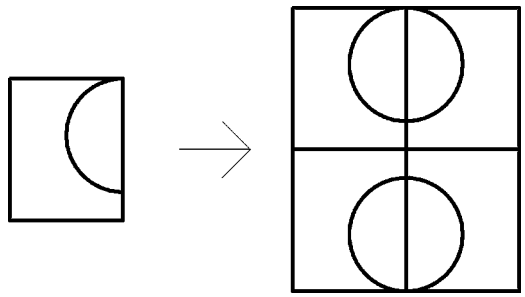

FIG. 1. Reflection and periodization of the image for convolution.

$$(p*x)[i,j]=\sum_{k=-K}^{K}\sum_{\ell=-K}^{K}p[k,\ell]x[i-k,j-\ell]. \tag{2}$$

Here we use the normalization

$$\sum_{k=-K}^{K}\sum_{\ell=-K}^{K}p[k,\ell]=1-c \tag{3}$$

to ensure the conservation of energy (in the case $\varepsilon=0$): $\Sigma_{i,j}m[i,j]^2=\Sigma_{i,j}x[i,j]^2$. Note that p is typically a smooth function with broad tails and so the convolution $p*x$ needs to be carefully defined near the boundary. Our approach is to reflect the image as shown in Fig. 1 and assume periodicity. Physically, this means that some scatter comes from outside of the image near the boundaries with tissue. This approach is an alternative to Ref. 4 for dealing with a finite image field.

Real-world mammograms differ from ideal mammograms in at least two ways: there is the open field consisting of radiation not penetrating the breast and the thickness of the breast is not constant (instead, it falls rapidly to zero near the boundary of the breast). The model (1) cannot simulate the high photon counts detected near the skinline in mammograms. We introduce a refinement of model (1) to deal with these unidealities.

We segment the mammogram into three disjoint regions (see Fig. 2):

(i) Open field,
(ii) region of varying thickness, and
(iii) region of constant thickness.

Consider the model

$$m=\chi+\tilde{c}x+\mathcal{P}(x)+\varepsilon, \tag{4}$$

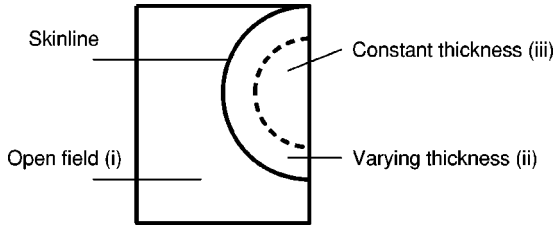

FIG. 2. Segmentation of the mammogram to three regions: (i) Open field; (ii) region of varying thickness; and (iii) region of constant thickness.

where

- χ is the open field which is constant in region (i) and zero in regions (ii) and (iii);
- $\tilde{c}$ is the spatially varying fraction of primary radiation. In region (iii) we set $\tilde{c}=c$ as in model (1) corresponding to the breast thickness in region (iii). In region (ii) $\tilde{c}$ is interpolated between c and zero according to the thickness at each point.
- $\mathcal{P}$ is a scattering operator with spatially varying PSF computed similarly to $\tilde{c}$ above.

Model (4) has the drawback that the scatter point spread function is no longer spatially invariant. The original motivation of Seibert and Boone in Ref. 4 was to introduce a computationally efficient scattering model based on convolution with a spatially invariant scatter PSF. However, we will later see that the scattered field produced by model (4) can be approximately restored by an algorithm using spatially invariant PSF.

B. Experimental determination of the scatter PSF

For practical use of the model (1), the scatter PSF p and the parameter c must be determined from experimental data. Originally, Seibert and Boone used a parametrized Gaussian scatter PSF.[4] This approach was improved in Ref. 5 by introducing an edge spread function (ESF) method. Similar methods (without the scattering medium) have been used to measure pure x-ray system impulse response.[7,8]

The idea is to measure the scatter ESF with an edge phantom and compute the spatial slit impulse response, or the scatter line spread function (scatter LSF). The rotationally symmetric scatter PSF can then be determined from the scatter LSF, as shown below.

The procedure of finding the scatter LSF from the measured ESF was only briefly discussed in Ref. 5. However, it is a delicate step since it involves the differentiation of noisy data. In the following, we present a robust ESF-to-LSF algorithm based on Tikhonov regularization.

1. Measuring scatter ESF

Our setup consists of a mammography x-ray source equipped with a full field digital detector,[9] lucite attenuators and an edge spread device (ESD). The mammography system has a source-to-image receptor distance (SID) of 645 mm, constant air gap between ESD and detector surface of 24 mm, molybdenum (Mo) anode and Mo-filter. No compression paddle or anti-scatter grid is used. The total thickness of carbon fiber at breast support is 3 mm. Manual kV settings of the x-ray source are 25, 26 and 28, and the exposure range is 32–50 mAs.

We use a direct flat panel detector based on amorphous selenium (a-Se). The pixel pitch is 85 μm and the image size is 2816×2048. The x-ray field is collimated to a detector area of 17.4 cm$\times$23.9 cm. Due to high inherent resolution of the direct detector, one is able to detect 42% signal at Nyquist limit (5.88 lp/mm).[6] The low-frequency scatter signal is well passed through the detection stage. Raw 16-bit images having 13-bits of image data are properly flat field corrected to eliminate image noise due to dark current, pixel defects

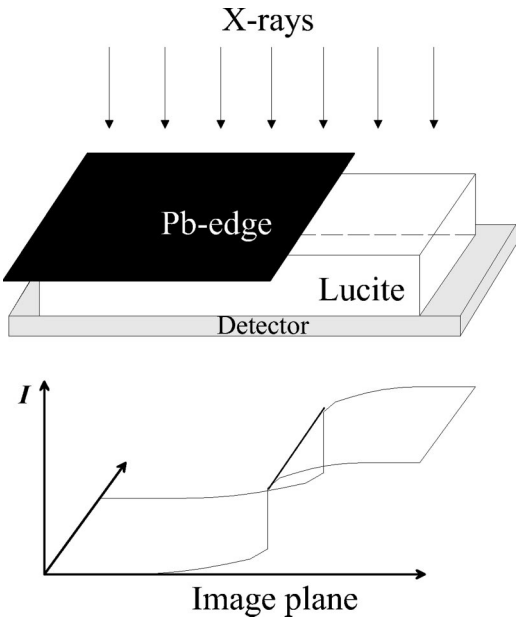

FIG. 3. ESF measurement.

and unequalities in pixel gains and offsets. No further image processing is applied to these technical raw images when scatter ESFs are to be determined.

The ESD is a device fabricated from a 1 mm thick lead (Pb) plate. The ESD is carefully set on top of the carbon fiber cover of the x-ray device having its straight-cut edge oriented parallel to the anode–cathode axis and situated directly under the focal spot. The position of the edge is constant during the measurements. The proper alignment of the edge is confirmed by checking the symmetry of ESF relative to the edge. The unsymmetric ESF would rise from the penumbral effect.

Lucite was used here to simulate the average breast tissue even though it has a higher attenuation coefficient (64% glandular) as the average (50% glandular) breast tissue. In future ESFs should be measured to each breast thickness and composition at several kVp settings.

See Fig. 3 for an illustration of the measurement setup.

2. Determining scatter LSF

Consider first the ideal ESF at the continuous limit (infinitesimal pixel size). Let $E(t)$ be a continuous, non-noisy profile from an ESF phantom image. Here we use the normalization $0 \leqslant t \leqslant 1$. We assume that $E(t)$ is of the form

$$E(t) = g(t) + \gamma\chi(t), \tag{5}$$

where

- $g(t)$ is the scatter ESF (a smooth function);
- $\chi(t)$ is a step function satisfying $\chi(t)=0$ for $t \leqslant \tilde{t}$ and $\chi(t)=1$ for $t > \tilde{t}$ (the image of the lead edge is at $t = \tilde{t}$);
- $\gamma > 0$ is the height of the vertical jump at the image of the edge. The fraction c of primary radiation under the lucite is then given by $c = \gamma / E(1)$.

Denote the scatter LSF by $f(t)$. It is the derivative of the scatter ESF:

$$f(t) = \frac{dg}{dt} = \frac{d}{dt}(E(t) - \gamma\chi(t)). \tag{6}$$

Integrating both sides of (6) leads to

$$\int_0^t f(s)ds = E(t) - \gamma\chi(t) + C, \tag{7}$$

where C is a constant of integration. We assume that $f(0) = 0$, so $C = 0$.

We turn to realistic discrete ESFs. We have available a noisy measurement μ_k of $E(t)$:

$$\mu_k = E(t_k) + \varepsilon_k, \tag{8}$$

where $t_k = (k-1)/(K-1)$ for $k = 1, \ldots, K$, and ε_k is a normally distributed random variable (noise). We have the following discrete version of (7):

$$\mu_k \approx \gamma\chi_k + \varepsilon_k + \frac{1}{K}\sum_{j=1}^{k} f_j, \tag{9}$$

where $f_j = f(t_j)$ and $\chi_k = \chi(t_k)$. Note that $\chi_k = 1$ for $k > \tilde{k}$ and $\chi_k = 0$ otherwise. The index $\tilde{k}$ is the largest number satisfying $t_{\tilde{k}} \leqslant \tilde{t}$. Given the vector $\mu = [\mu_1, \ldots, \mu_K]^T$ we want to determine the vector $f = [f_1, \ldots, f_K]^T$ and the scalar γ. We write conditions (9) in matrix form:

$$\mathbf{A}\begin{bmatrix} f \\ \gamma \end{bmatrix} = \mu - \varepsilon, \tag{10}$$

where the matrix $\mathbf{A}$ has size $K \times (K+1)$ and is given by

$$K\mathbf{A} = \begin{bmatrix} \underset{\tilde{k}\times\tilde{k}}{\mathbf{L}} & \underset{\tilde{k}\times(K-\tilde{k})}{\mathbf{0}} & \underset{\tilde{k}\times 1}{\mathbf{0}} \\ \underset{(K-\tilde{k})\times\tilde{k}}{\mathbf{1}} & \underset{(K-\tilde{k})\times(K-\tilde{k})}{\mathbf{L}} & \underset{(K-\tilde{k})\times 1}{K\mathbf{1}} \end{bmatrix}. \tag{11}$$

Here $\mathbf{1}$ denotes an all-one matrix, $\mathbf{0}$ an all-zero matrix and $\mathbf{L}$ a lower triangular matrix of the form

$$\mathbf{L} = \begin{bmatrix} 1 & 0 & \ldots & 0 & 0 \\ 1 & 1 & \ldots & 0 & 0 \\ \vdots & \vdots & \ddots & \vdots & \vdots \\ 1 & 1 & \ldots & 1 & 0 \\ 1 & 1 & \ldots & 1 & 1 \end{bmatrix}. \tag{12}$$

The matrix equation (10) is ill-conditioned because it implements the differentiation of noisy data. We regularize the solution by introducing four types of *a priori* information on f and γ:

(1) Vanishing at endpoints: $f_1 = 0 = f_K$;
(2) smoothness: $f_k \approx f_{k+1}$;
(3) symmetry: $f_{\tilde{k}+\ell} = f_{\tilde{k}-\ell}$,

(4) the number γ is near an initial guess: $\gamma \approx \gamma_0$.

We write (1)–(4) in matrix form:

$$\mathbf{B}\begin{bmatrix} f \\ \gamma \end{bmatrix} = \begin{bmatrix} 0 \\ \gamma_0 \end{bmatrix}, \tag{13}$$

where $\mathbf{B} = [B_1^T B_2^T B_3^T B_4^T]^T$ and

$$B_1 = \begin{bmatrix} 0 & 0 & \cdots & \alpha_1 & 0 \\ \alpha_1 & 0 & \cdots & 0 & 0 \end{bmatrix},$$

$$B_2 = \begin{bmatrix} \alpha_2 & -\alpha_2 & 0 & \cdots & 0 & 0 & 0 \\ 0 & \alpha_2 & -\alpha_2 & \cdots & 0 & 0 & 0 \\ \vdots & \vdots & \ddots & \ddots & \ddots & & \vdots \\ 0 & 0 & 0 & \cdots & \alpha_2 & -\alpha_2 & 0 \end{bmatrix},$$

$$B_3 = \begin{bmatrix} 0 & \cdots & \alpha_3 & 0 & -\alpha_3 & \cdots & 0 & 0 \\ \vdots & & & \vdots & & \ddots & \vdots & \vdots \\ \alpha_3 & \cdots & 0 & 0 & 0 & \cdots & -\alpha_3 & 0 \end{bmatrix},$$

$$B_4 = [0 \ \cdots \ 0 \ 1].$$

The numbers $\alpha_1, \alpha_2, \alpha_3$ are positive regularization parameters. As explained by Varah,[10] a regularized solution of (10) is given by the least-squares solution of the following overdetermined set of linear equations:

$$\begin{bmatrix} \mathbf{A} \\ \mathbf{B} \end{bmatrix}\begin{bmatrix} f \\ \gamma \end{bmatrix} = \begin{bmatrix} \mu \\ 0 \\ \gamma_0 \end{bmatrix}. \tag{14}$$

We note that the above algorithm is a special case of Tikhonov regularization.[11]

We can add stability to the computation by using multiple measurements: each row of the ESF image is an independent noisy ESF measurement. We can utilize several rows, denoted by $\mu^{(1)}, \ldots, \mu^{(M)}$, by solving the following modification of (14):

$$\begin{bmatrix} \mathbf{A} \\ \vdots \\ \mathbf{A} \\ \mathbf{B} \end{bmatrix}\begin{bmatrix} f \\ \gamma \end{bmatrix} = \begin{bmatrix} \mu^{(1)} \\ \vdots \\ \mu^{(M)} \\ 0 \\ \gamma_0 \end{bmatrix}. \tag{15}$$

Another approach would be to substitute the average of the M rows in place of μ in (14), but we are in favor of not manipulating the raw data before inversion.

3. Determining scatter PSF and its Fourier transform

Scatter LSF and PSF are functions of one and two variables, respectively: $f = f(\cdot)$ and $p = p(\cdot,\cdot)$. Assuming p is rotationally symmetric we have

$$f(t) = \int_{-\infty}^{\infty} p(t,\lambda)\, d\lambda.$$

Fourier transforming f yields

$$\begin{aligned} \hat{f}(s) &= \int_{-\infty}^{\infty} e^{-ist} f(t)\, dt \\ &= \int_{-\infty}^{\infty}\int_{-\infty}^{\infty} e^{-ist} p(t,\lambda)\, dt\, d\lambda \\ &= \int_{-\infty}^{\infty}\int_{-\infty}^{\infty} e^{-i(s,0)\cdot(t,\lambda)} p(t,\lambda)\, dt\, d\lambda = \hat{p}(s,0). \end{aligned} \tag{16}$$

Since p is rotationally symmetric, so is $\hat{p}$. Thus the profile (16) completely determines $\hat{p}$. The scatter PSF is easily computed from $\hat{p}$ by 2D inverse Fourier transform.

C. CNR of gridless digital mammograms

Since the scattered field is a low-frequency signal, gray-scale optimization eliminates scatter artifacts from gridless digital mammograms. Therefore an absolute determination of the scattered field is not necessary for the optimal viewing of mammograms. However, x-ray scattering decreases contrast resolution in an image, as discussed by Barnes.[12]

Contrast resolution is defined as the relative difference of an object signal level compared to the background signal. The greater the signal step, the better the contrast of the imaged object. The following approach describes under what circumstances the grid can be removed while maintaining image quality in terms of the contrast-to-noise ratio (CNR).

Compare an imaging setup where an ideal grid is used versus a situation where the grid is removed. (Here an *ideal grid* has 100% transmission of primary radiation and 0% transmission of scattered radiation.) Having the same detector entrance dose, the total signal in the latter case is composed of both scattered and primary radiation. Therefore, the object CNR with an ideal grid is greater due to a higher primary signal. Even though we would use the scatter removal algorithm, a lower primary signal level and lower CNR would exist without an efficient noise removal algorithm. Thus, we have to increase the amount of primary radiation detected which is possible in digital mammography due to the wider dynamic range of the digital detector. The problem in screen-film mammography is the relatively narrow dynamic range which does not enable the detection of both the primary and the scattered radiation.

In practice, anti-scatter grids are not ideal. The grid ratio, or the relation of the height of the lead strips to the distance between them, increases the transmission of scattered radiation to 10%–20%. Accordingly, the Pb strips absorb primary radiation 20%–50%. Two questions arise when an unideal grid is removed:

(a) How much can we reduce patient dose without decreasing CNR?
(b) While maintaining the patient dose, how much can we increase image quality, i.e., enhance diagnostic information, in terms of CNR?

The following analysis defines the theoretical scatter fraction threshold below which CNR in a gridless image taken by a certain patient dose reduction is equal or higher than in an image taken with the grid. The images are acquired from

the same low-contrast object having contrast or image signal step depth proportional to primary radiation on the detector. Let us denote grid transmission factors for primary radiation and scattered radiation by α and β, respectively. Also, we denote by d the fraction of the original patient dose used. CNRs for images taken with (G) and without a grid (NG) are

$$(C/N)_G = \frac{\text{step}_G}{f\sqrt{P_G + S_G}}, \tag{17}$$

$$(C/N)_{NG} = \frac{\text{step}_{NG}}{f\sqrt{P_{NG} + S_{NG}}}, \tag{18}$$

where f is a device dependent constant. Thus, one must find a solution to $(C/N)_{NG} \geqslant (C/N)_G$.

When P and S are the primary and the scatter components on the grid, corresponding components below the grid are $P_G = \alpha P$ and $S_G = \beta P$. The primary and the scatter components in the gridless image depend on dose reduction by $P_{NG} = d \cdot P$ and $S_{NG} = d \cdot S$. Thus, we can write

$$\text{step}_{NG} \geqslant \text{step}_G \frac{\sqrt{dP + dS}}{\sqrt{\alpha P + \beta S}}. \tag{19}$$

Using $\text{step}_{NG} = \text{step}_G (d/\alpha)$ and the definitions of the primary-to-scatter ratio $\text{psr} = P/S$ and scatter fraction $\text{sf} = S/(S+P)$, we get the threshold scatter fraction:

$$\text{sf} = \left(1 + \frac{\alpha^2 - d\beta}{d\alpha - \alpha^2}\right)^{-1}. \tag{20}$$

D. Determining the scattered field

1. Ideal mammograms

Assume given a mammogram m of the form (1) and the model parameters p, c. We wish to compute the scattered field $p * x$. Then the scatter-free image x is determined up to noise by the formula

$$x + c^{-1}\varepsilon = c^{-1}m - c^{-1}(p * x). \tag{21}$$

Fourier transforming (1) leads to

$$\hat{x} = \frac{\hat{m}}{c + \hat{p}} - \frac{\hat{\varepsilon}}{c + \hat{p}}. \tag{22}$$

Typically, $\hat{p}$ is real-valued and non-negative, so division by $c + \hat{p}$ in (22) is justified. Multiplying (22) by $\hat{p}$ gives

$$\hat{p}\hat{x} = \frac{\hat{p}\,\hat{m}}{c + \hat{p}} - \frac{\hat{p}\,\hat{\varepsilon}}{c + \hat{p}} \approx \frac{\hat{p}}{c + \hat{p}}\hat{m}, \tag{23}$$

the latter approximate equality coming from the fact that ε is zero-centered, low-amplitude white noise and $\hat{p}$ is concentrated on low frequencies.

We reconstruct approximately the scattered field using formula (23) and the inverse Fourier transform:

$$s = \mathcal{F}^{-1}\left(\frac{\hat{p}}{c + \hat{p}}\hat{m}\right). \tag{24}$$

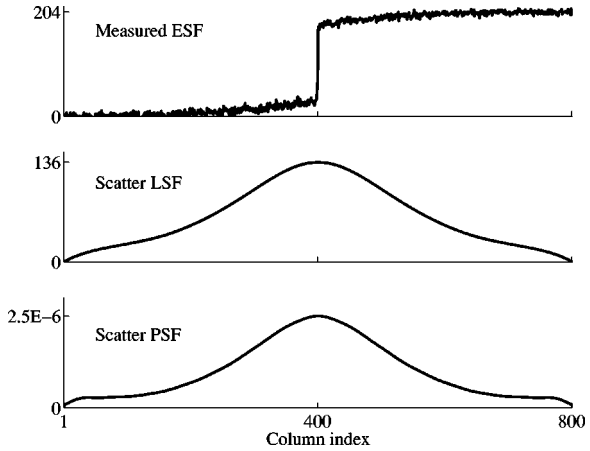

FIG. 4. Top: Row of the measured ESF image. Compare to Fig. 3. Middle: Scatter LSF by regularized computation. Bottom: Profile of the rotationally symmetric 2D scatter PSF.

Remark: Gonzàlez Trotter *et al.* presented in Ref. 13 an iterative algorithm for determining the scattered field. Due to convergence problems, they needed to introduce certain technical details to overcome the case $c \geqslant 1/2$. The present algorithm is applicable with any $0 < c < 1$.

2. Approximate method for real mammograms

Given a full-field digital mammogram, we perform the following steps:

(1) Find the skinline.
(2) Subtract the open field.
(3) Find the maximum pixel value $p_{\max}$ in the region (iii) of constant breast thickness. Set all pixel values greater than $p_{\max}$ equal to $p_{\max}$.
(4) Recover the scattered field approximately by inserting the outcome of step (3) in place of m in (24). Here p and c correspond to model (1) for breast thickness in region (iii).

Note that $p * x$ contains only very low frequencies and is thus completely determined by its downsampled version by the Whittaker–Shannon sampling theorem. Thus the mammogram can be downsampled before step (3) and the recovered scattered field again upsampled after step (4). This speeds up the computation considerably.

III. RESULTS

A. Experimental determination of the scatter PSF

To measure the scatter ESF, acrylic slabs were positioned under the ESD and edge profiles were acquired. The following combinations of kVps and acrylic slab thicknesses were used: 25 kVp: 30 mm, 40 mm; 26 kVp: 70 mm; 28 kVp: 40 mm, 50 mm, 60 mm, 70 mm.

See the top graph in Fig. 4 for a measured ESF with acrylic thickness 30 mm and exposure parameters 25 kVp

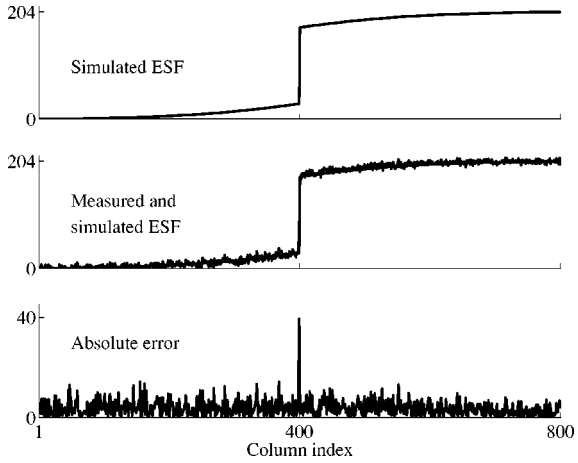

FIG. 5. Top: Row of the simulated ESF image. Middle: Superposition of corresponding rows of the measured and simulated ESF images. Bottom: Absolute value of the difference between measured and simulated ESF. The peak at the lead edge results from imperfect alignment of the edge with the pixels.

and 32 mAs. The image was truncated to a width of 801 pixels so that the edge was approximately on the middle column.

Scatter LSF was determined by inserting seven rows of the above ESF image into (15), so we had $M=7$, $K=801$ and $\tilde{k}=401$. Regularization parameters were $\alpha_1=\alpha_2=\alpha_3=10$. An initial approximation $\gamma_0=140$ was read from the ESF image, and the result of the computation was $\gamma=145.4$. An estimate for $E(1)$ was achieved by averaging values of the measured ESF near the boundary, leading to $c=0.71$. The Fourier transform of the scatter PSF was computed using (16). The function p was then achieved by 2D inverse Fourier transformation. See Fig. 4.

The scatter PSF was tested by simulating an edge phantom image as a piecewise constant function having value zero under the imaginary lead plate and $E(1)$ elsewhere. This image was convolved with the scatter PSF to simulate the scattered field. As seen in Fig. 5, the model is in reasonable agreement with the measurement.

TABLE I. Scatter fractions at different breast thicknesses.

kVp	2 cm	4 cm	6 cm	8 cm
0% glandular				
24	.21	.29	.43	.66
28	.17	.28	.36	.47
32	.18	.29	.35	.42
36	.19	.29	.36	.43
43% glandular				
24	.18	.30	.47	
28	.17	.26	.35	
32	.17	.26	.35	.42
36	.18	.28	.36	.42
100% glandular				
24	.18	.35		
28	.18	.30	.47	
32	.17	.27	.40	.51
36	.19	.29	.38	.47

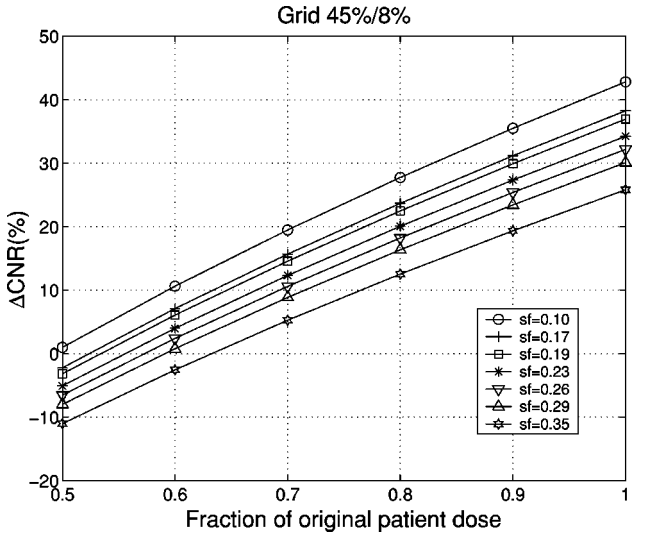

FIG. 6. Relative change in CNR at different patient dose reductions. The grid has a 45% primary transmission factor and 8% scatter transmission factor. Calculations are done with an object having a contrast of 4%.

B. CNR of gridless digital mammograms

Table I presents scatter fractions calculated from the results of Ref. 5. They are calculated for different breast thicknesses and glandular compositions at several kVps and 10 cm×10 cm x-ray field.

To answer questions set earlier in this sections, see Figs. 6–9. Values for α and β are set according to Gilardoni specifications for GRIDGIL mammographic grids.

(a) According to our analysis the patient dose can be reduced without degrading the image quality from 11.7% up to 47.2% at breast thickness of 2 cm and from 0.1% up to 40.8% at breast thickness of 4 cm depending on the grid.

(b) The increase in CNR is from 6.3% up to 37.5% at breast thickness of 2 cm and from 0.4% up to 30.0% at a breast thickness of 4 cm.

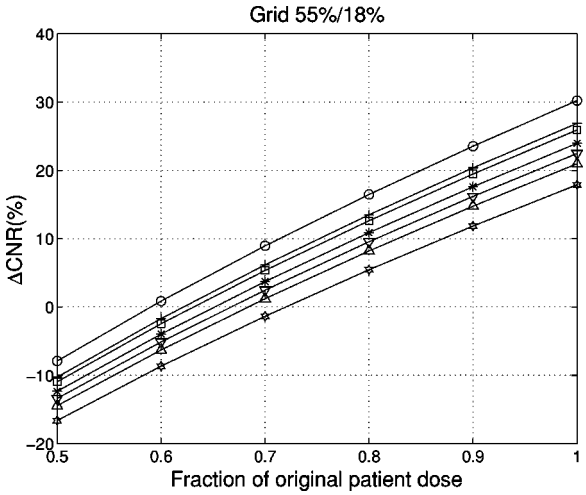

FIG. 7. The relative change in CNR at different patient dose reductions. The grid has a 55% primary transmission factor and 18% scatter transmission factor. Calculations are done with an object having a contrast of 4%. For symbols, see Fig. 6.

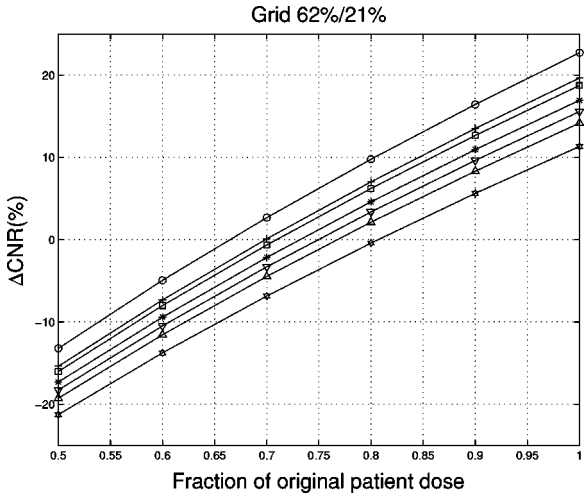

FIG. 8. The relative change in CNR at different patient dose reductions. The grid has 62% primary transmission factor and 21% scatter transmission factor. Calculations are done with object having contrast of 4%. For symbols, see Fig. 6.

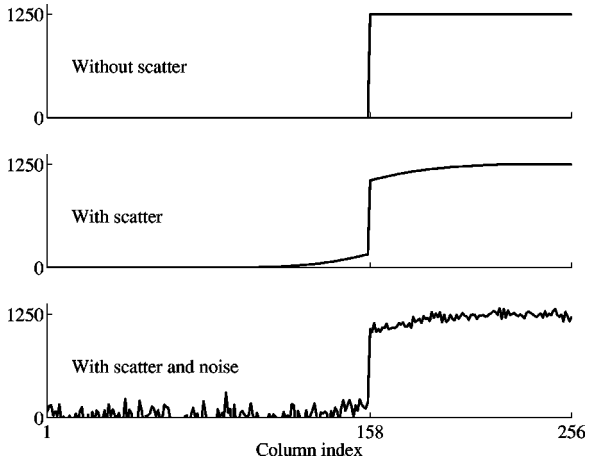

FIG. 10. Top: Row 128 of the ideal scatter-free mammogram x. Middle: row 128 of the scatter-degraded image $cx+p*x$. Bottom: row 128 of the simulated noisy mammogram $m=cx+p*x+\varepsilon$, where the noise level outside the skinline is thought to result from removed open field.

C. Computation of scattered fields

1. Simulated ideal mammogram

We build a simulated image of size 256×256 according to model (1). The form of the simulated 30 mm thick breast is taken to be a half-circle. We assume that the half-distance of the X-radiation is 10 mm and that the unattenuated photon count at each pixel would be $I_0=10000$ photons. Under the area of the breast having a thickness of three half-lengths, pixel values are proportional to the photon count $I_0/8=1250$ in the non-noisy scatter-free image x. For simplicity, we take pixel values to be equal to photon counts; this assumption is not crucial for the algorithms. See the top plot in Fig. 10.

To simulate the primary field cx, we take $c=0.71$. Consider the scatter PSF shown in Fig. 4. We dilate this p so that the diameter of its support becomes 128 pixels and normalize it so that its total mass is $1-c=0.29$. Using FFT and the reflection shown in Fig. 1, we compute the simulated scattered field $p*x$. See Figs. 10 and 11.

The amplitude of noise is chosen to approximate the Poisson statistics of x-ray measurements: we add to each pixel a Gaussian zero-centered random error with variance equal to the pixel value. In addition, we put some noise outside the breast, too. This is for simulating the situation where the open field has been removed from a measured mammogram, and thus we choose the standard deviation of the noise to be $\sqrt{I_0}=100$. See the bottom plot in Fig. 10.

The scattered field was recovered by formula (24); see Fig. 11. Relative errors of the reconstruction in the energy norm and supremum norm are

$$\frac{\|p*x-s\|_2}{\|p*x\|_2}=0.3\%, \qquad \frac{\max|p*x-s|}{\max|p*x|}=0.4\%.$$

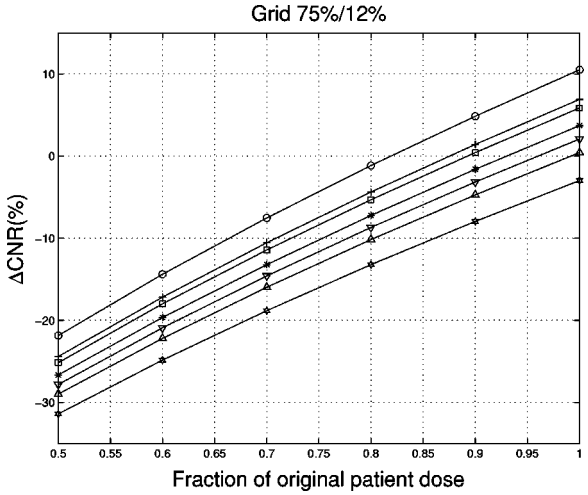

FIG. 9. Relative change in CNR at different patient dose reductions. The grid has 75% primary transmission factor and 12% scatter transmission factor. Calculations are done with an object having a contrast of 4%. For symbols, see Fig. 6.

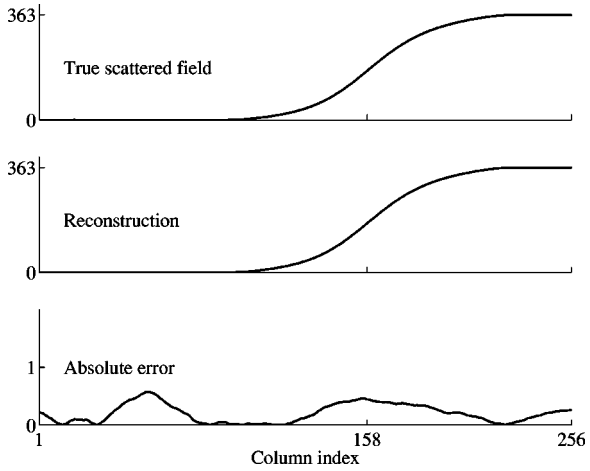

FIG. 11. Top: row 128 of the simulated scattered field. Middle: row 128 of the reconstructed scattered field. Bottom: row 128 of the absolute value of the difference between a true and reconstructed scattered field.

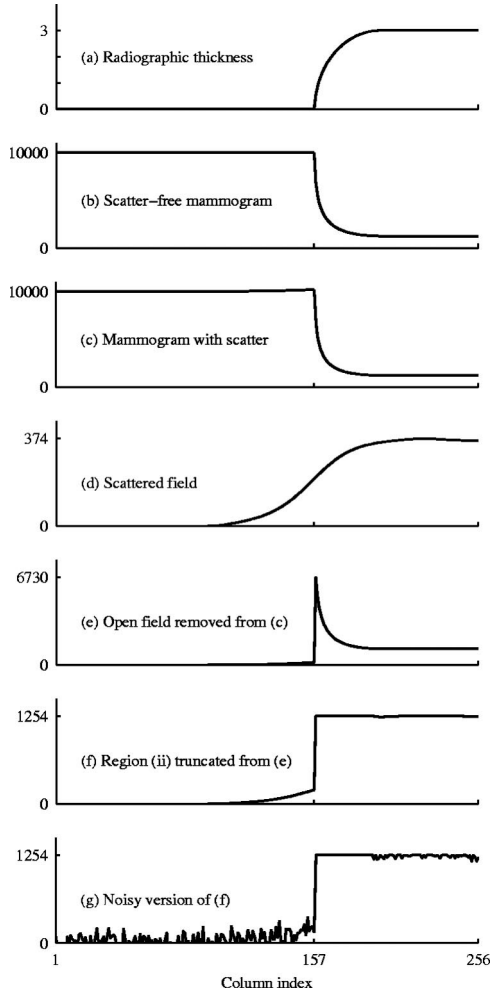

FIG. 12. An illustration of scatter-free and scatter-degraded simulated mammograms. Scattering is simulated according to model (4) using a spatially varying scatter PSF. In all the graphs, the skinline is at the column 157. Graphs from top to bottom: (a) Radiographic thickness profile of the breast (units in half-lengths). (b) Pixel values along row 128 in a scatter-free mammogram. (c) Pixel values along row 128 of a mammogram with scattering. (d) A profile of the scattered field along row 128. (e) As in (c), but with the open field removed. (f) As in (e), but region (ii) truncated according to step (3) in the determination of the scattered field. (g) As in (f), but modeling measurement noise.

2. Simulated mammogram

We simulate a mammogram according to model (4). The thickness of the simulated breast in region (iii) of Figure 2 is taken to be 30 mm. We assume that the half-distance of the X-radiation is 10 mm and that the unattenuated photon count at each pixel would be $I_0=10000$ photons.

First, we construct the scatter-free mammogram,

$$x+\chi.$$

- In region (iii), only one out of eight photons makes it through the tissue since the thickness is three half-lengths. Thus $x[i,j]=I_0/8$ in region (iii). In region (ii), we compute $x[i,j]$ by the standard exponential attenuation law.
- The open field χ is constructed as $\chi[i,j]=I_0$ in region (i) and $\chi\equiv 0$ in regions (ii) and (iii).

Second, we introduce scatter to construct

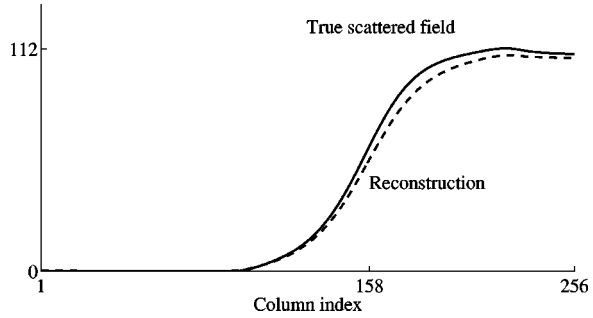

FIG. 13. Solid line: row 128 of the true scattered field. Dashed line: row 128 of the approximate reconstruction from simulated noisy mammogram of breast with varying thickness.

$$\chi+\tilde{c}x+\mathcal{P}(x).$$

- In region (iii) compute the primary field by $(\tilde{c}x)[i,j]=0.71\cdot x[i,j]$. In region (ii) set $(\tilde{c}x)[i,j]=\tilde{c}[i,j]\cdot x[i,j]$, where $\tilde{c}[i,j]$ is interpolated between 0 and 0.71 according to the thickness of the breast at pixel $[i,j]$.
- In region (iii) the scattered field $\mathcal{P}(x)$ is modeled by adding to the image the scatter PSF p (of mass 0.29) with the center at the pixel in question. In region (ii) we add to the image the scatter PSF normalized to mass $1-\tilde{c}[i,j]$ with the center at the pixel in question. We use the reflection depicted in Fig. 1 to take the boundaries into account. Here we ignore the possible change in the *form* of the scatter PSF and only change its *mass*. In region (i), there is no scattering (scatter PSF$\equiv 0$), but the effect of scattering in regions (ii) and (iii) increases the photon count near the skinline in region (i).

Third, we add noise. See Fig. 12.

See Fig. 13 for the reconstruction of scattered field with steps (1)-(4). Relative errors of the reconstruction in energy norm and supremum norm are

$$\frac{\|\mathcal{P}(x)-s\|_2}{\|\mathcal{P}(x)\|_2}=7.3\%, \qquad \frac{\max|\mathcal{P}(x)-s|}{\max|\mathcal{P}(x)|}=16.5\%.$$

We remark that the intuitive idea behind this method is the similarity of the middle graph in Fig. 10 and graph (f) in Fig. 12.

3. Clinical mammogram

Here the scatter removal steps are performed to a real clinical full-field digital mammogram acquired without a grid. The exposure parameters for the 3 cm breast are 25 kVp, 32 mAs, and Mo–Mo anode–filter combination. Thus, we can still utilize the same PSF as before.

Figures 14 and 15 demonstrate that one subtracts nearly a constant or at least an extremely low-frequency offset from a real mammogram therefore causing no fine-detail information loss. This procedure is done when optimizing digital mammograms for softcopy or hardcopy reading and no further scatter removal is needed.

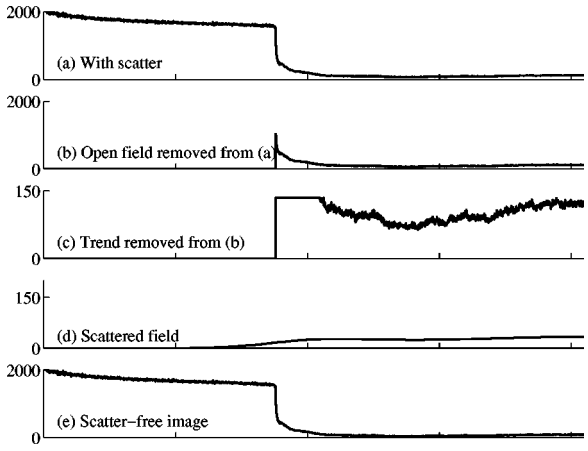

FIG. 14. Results for a clinical mammogram. In all the graphs the position of the skinline is constant. Graphs from top to bottom: (a) Profile of a gridless clinical mammogram. The open field yields to a higher signal level. The profile is taken at the anode–cathode direction and the increasing trend due to the heel effect is seen. (b) The signal outside the skinline is segmented out. (c) A breast thickness related trend is removed by clipping the pixel values above a threshold. (d) The scatter field calculated from (c). (e) The corresponding profile of the scatter-free image.

IV. DISCUSSION

We considered the scattering model of Boone and Seibert and introduced a robust algorithm for finding the model parameters from ESF measurements. Using the scattering model, we studied two questions related to gridless digital mammography.

First, we discussed the implications of the scattering model to the CNR of the gridless digital mammograms. We noted that the low-frequency scattered field is eliminated by any trend removal algorithm needed to optimize the gray levels of a digital mammogram for viewing. However, detecting the scattered field uses part of the dynamic range of the detector, and this affects the CNR. Our results suggest that, for breast thickness between 20-40 mm, the CNR is improved by 0.4-6.3% while patient dose is decreased 0.1-11.7%. These results apply to removing the most efficient grid commercially available.

However, the above results are direct mathematical consequences of the scattering model. In practical imaging situations the model holds only approximately, and the actual improvement of perceived image quality by removing the grid needs to be checked by a clinical study.

Second, we discussed the determination of the scattered field given a digital gridless mammogram and imaging parameters. This is needed, e.g., in 3D mammography to convert photon count images into tomographic data. We presented a fast and robust algorithm for approximate determination of the scattered field. Our algorithm requires as preprocessing steps finding the skinline, removing the open field and cutting away pixel values above a certain threshold. While these steps are by no means trivial to implement, they can be viewed as necessary algorithms in any reasonable digital processing system for full-field digital mammograms. The method was tested on a simulated mammogram produced with an extension of the Boone–Seibert model. The relative square error of the reconstruction was 7.6%. Also, we applied the method to a clinical full-field digital mammogram and concluded that the algorithm is fast enough for clinical use.

In the derivation of the algorithm, a couple of simplifying assumptions were made. Interpolation of the scatter PSF between the full-thickness PSF and zero could be replaced by a sequence of PSF's corresponding to various intermediate thicknesses. Further, the reflection depicted in Fig. 1 is not necessarily modeling adequately the scattering from outside the image area: beam collimation reduces the intensity of x-rays inside the tissue outside the compressed breast, and only multiple scattering from that tissue can be detected.

The simulation of the test mammogram also has some unrealistic assumptions. We ignored the heel effect by assuming that the open field is constant, and the scatter PSF was rotationally symmetric even in the nonsymmetric region (ii). Thus the promising result of this simulation needs further verification by comparing reconstructions to practically measured scattered fields. This is left to a future study.

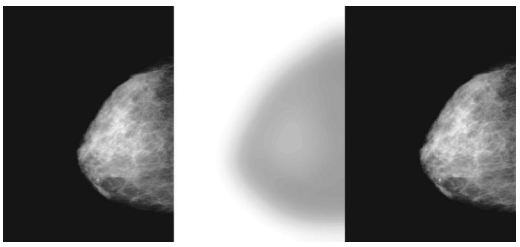

FIG. 15. A clinical mammogram before and after scatter removal. In these images white refers to low and black to high photon count. Windowing and gamma correction is applied on images. Left: original mammogram with scattering. Middle: the removed scattered field (grayscale is exaggerated for clarity) Right: mammogram without scattering.

ACKNOWLEDGMENTS

The authors would like to thank Martti Pamilo, MD, Ph.D., Section Head, Helsinki University Central Hospital, Mammography Department, for making the clinical images available. Also, the authors are grateful to the referees for their helpful comments.

[a]Electronic mail: kirsi.nykanen@fi.instrumentarium.com

[1] J. V. Lacey, S. S. Devesa, and L. A. Printon, "New trends in breast cancer incidence and mortality," Environ. Mol. Mutagen. **39**(2–3), 82–2 (2002).
[2] R. T. Greenlee, T. Murray, S. Bolden, and P. A. Wingo, "Cancer Statistics, 2000," Ca-Cancer J. Clin. **50**, 7–33 (2000).
[3] J. M. Boone, K. K. Lindfors, V. N. Cooper, III, and J. S. Seibert, "Scatter/primary in mammography: Comprehensive results," Med. Phys. **27**, 2408–2416 (2000).
[4] J. A. Seibert and J. M. Boone, "X-ray scatter removal by deconvolution," Med. Phys. **15**, 567–575 (1988).
[5] V. N. Cooper, J. M. Boone, J. A. Seibert, and C. J. Pellot-Bakarat, "An edge spread technique for measurement of the scatter-to-primary ratio in mammography," Med. Phys. **27**, 845–853 (2000).
[6] B. Polischuk, S. Savard, V. Loustauneau, M. Hansroul, S. Cadeux, and A. Vague, "Se-based flat panel detector for screening mammography,"

Physics of Medical Imaging, Medical Imaging 2001, San Diego, Proceedings of SPIE, Volume 4320, pp. 582–589.
[7] H. Fujita, D. Tsai, T. Itoh, K. Doi, J. Morishita, K. Ueda, and A. Ohtsuka, ''A simple method for determining the modulation transfer function in digital radiography,'' *IEEE Transactions on Medical Imaging*, Vol. 11, pp. 34–39.
[8] E. Samei, M. J. Flynn, and D. A. Reimann, ''A method for measuring the presampled MTF of digital radiographic systems using an edge test device,'' Med. Phys. **25**, 102–109 (1998).
[9] Diamond DX, Instrumentarium Corp. Imaging Div., Tuusula, Finland.
[10] J. M. Varah, ''A practical examination of some numerical methods for linear discrete ill-posed problems,'' SIAM Rev. **21**, 100–111 (1979).
[11] A. N. Tikhonov, ''Solution of incorrectly formulated problems and the regularization method,'' Sov. Math. Dokl. **4**, 1035–1038 (1963).
[12] G. T. Barnes, ''Contrast and scatter in x-ray imaging,'' Radiographics **11**, 307–323 (1991).
[13] D. E. Gonzàlez Trotter, J. E. Tkaczyk, J. Kaufhold, B. E. H. Claus, and J. E. Eberhard, ''Thickness-dependent scatter correction algorithm for digital mammography,'' *Progress in Biomedical Optics and Imaging*, Vol. 3, No. 20; Medical Imaging 2002, San Diego, USA, *Proceedings of SPIE*, Vol. 4682, pp. 469–478.